ORIGINAL RESEARCH ARTICLE

Directional Solidification of Al–Si–Ti Irregular Ternary Eutectic Alloy and Thermophysical Properties

ÜMİT BAYRAM

Directional solidification of Al–11.75 wt pct Si–2.15 wt pct Ti irregular eutectic alloy which has an 843.83 K melting point, was done with different growth rates (V = 8.51 to 2065.18 μm s^{-1}) at a temperature gradient (G) of 8.36 K mm^{-1} using Bridgman-type directional solidification apparatus (BTDSA). Scanning electron microscopy (SEM)—Energy dispersive X-ray (EDX) and X-ray diffraction (XRD) were used to characterize all phases forming the alloy. The average values of interflake spacing (λ_T) were measured from transverse sections of the directionally solidified samples with standard techniques. The dependency of λ_T was experimentally obtained using linear regression analysis for low, high, and all growth rates. It was observed that the λ_T values tended to decrease with increasing V values; therefore, the interflake structures came closer. The fusion enthalpy (ΔH_f) and specific heat difference between solid and liquid (ΔC_p) for the Al–Si–Ti eutectic alloy were found as 376.12 J $g^{-1}$and 0.659 J g^{-1} K^{-1}, respectively, by the differential scanning calorimetry (DSC). All results obtained in the present work were compared with the eutectic theory and the Al-based similar experimental results in the literature.

ÜMİT BAYRAM is with the ERNAM-Erciyes University Nanotechnology Application and Research Center, 38039 Kayseri, Turkey and also with the AGU-CRF, Central Research Facility, Abdullah Gül University, 38080 Kayseri, Turkey. Contact e-mail: umit.bayram@agu.edu.tr

Manuscript submitted February 28, 2022; accepted September 4, 2022.

Article published online October 3, 2022.

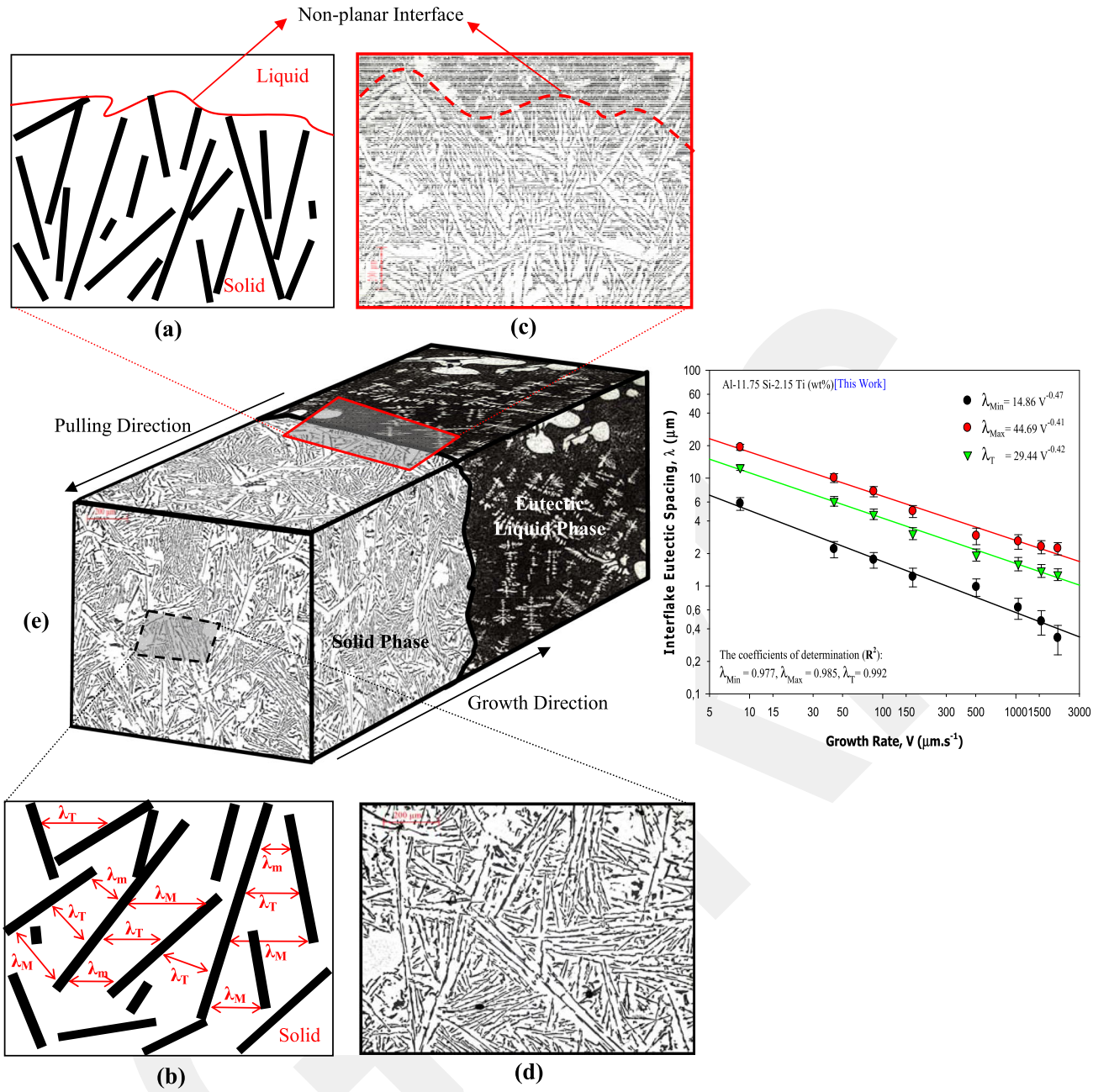

https://doi.org/10.1007/s11663-022-02648-6

I. INTRODUCTION

DIRECTIONAL solidification is used not only for producing and developing technologically essential alloys but also has become the focus of theoretical and experimental studies for researchers in recent years. This method helps understand the relationship between alloys and their microstructure, geometric structure, and production conditions. Controlling the nucleation and growth rates during solidification ensures the homogeneity and integrity of the solid material with its grain size and shape. Similarly, purification can be achieved by controlling the solidification rate. In addition, knowing the solidification mechanism directly affects the control of the materials' thermal, electrical, and mechanical properties.[1]

In the 1960s, the first study of directional solidification was carried out to produce turbine blades.[2] This method has been used in many studies to produce binary and ternary eutectic alloys in the literature until today.[3–25] Eutectic alloys are the base alloys preferred by researchers and the casting industry due to their casting abilities, low melting temperatures and superior mechanical properties.[26–29] The Bridgman-type directional solidification apparatus (BTDSA) is one of the main techniques used for directional solidification (crystal growth) of eutectic alloys. Undesirable casting defects such as distortion and cracks due to the stresses caused by aluminum and aluminum-based multiple alloys during volume reduction can be reduced to minimum levels using the Bridgman-type-controlled solidification technique which is given details in the References 30, 31.

To improve the mechanical properties and microstructure of cast alloys in different applications, many methods are preferred such as alloying,[32] heat treatment,[33] and hot deformation.[34] Comparing these methods, the alloying can provide a relatively simple and efficient approach to improve the mechanical properties of cast alloys and control the microstructure.[35] Al–Si eutectic alloys that are obtained through the alloying method are among the most popular aluminum-based casting alloys in the material world. Because many aluminum alloys used in the casting industry contain the element silicon as a basic alloy addition, these alloys also have properties such as high resistance to corrosion, high fluidity, reduction of shrinkage, low coefficients of thermal expansion, and good weldability.[36–39] Also, since silicon is a eutectic former in aluminum alloys, it provides sufficient fluidity to feed shrinkage in castings.[40] The first investigation in 1921 was the study by Pacz[41] that "The eutectic silicon phase in the aluminum alloy can be modified or refined by melting the alloy under sodium fluoride flow" so that the eutectic silicon phase can be observed. Refining the eutectic silicon structure by a modification to improve the mechanical properties of casting alloys has been widely preferred in the industry since the 1970s.[42]

Incorporation of Ti in potential industrial applications for cast aluminum alloys results in high-grain refinement efficiency and improved stability.[43] The presence of Titanium element, although the solubility value in Al-Si alloys is approximately 0.15 pct by mass, it makes an important contribution to solution hardening, grain refinement, and increasing tensile strength.[44–46] Adding Titanium to the Al–Si eutectic alloy increases the microhardness value of the binary alloy and improves the wear resistance of both cast and heat-treated alloys.[47] In addition, it is possible to improve both the wettability and the microstructure with a suitable combination of Ti content to be added to the Al–Si alloy.[48] Finally, in the presence of the Ti element, the resulting intermetallic phases after solidification in aluminum alloys have a strong effect on the mechanical properties of the materials.[49–51]

According to results from previous studies by scientists,[3–15,17,18,20,21,23,25] the studies on directional solidification were implemented mainly by using Bridgman-type equipment with a growth range of ~ 8.0 to 250.0 μm s^{-1} at a constant temperature gradient, and the effect of growth rate on the microhardness, ultimate tensile strength, microstructure parameters, and electrical properties were determined from experimental outcomes. In directional growth studies, it is also understood that it is more challenging to achieve controlled solidification with a growth rate higher than ~ 400.0 μm s^{-1}. During solidification, it is difficult to control the microstructure of the materials depending on the growth rate. In addition, the most important challenge during solidification is rapid phase growth. Due to the high diffusion coefficient in the liquid metal and the high supersaturation encountered in most alloys, the growth rate of the solidification front is very fast, from micrometers per second to millimeters per second.[52] It is also stated that high growth rates contribute significantly to the regional interfacial supercooling, and these changes can significantly change the region solidified by the rapid solidification process.[53]

Therefore, the present work aimed to experimentally search the dependencies of eutectic interflake spacings (λ) on high growth rates (higher than ~ 400.0 μm s^{-1}) as well as standard growth rates range in the literature at 8.36 K mm^{-1} (constant) in the Al–11.75 wt pct Si–2.15 wt pct Ti irregular eutectic alloy and compare the outcomes with previous experimental results for Al-based alloys. In addition, the main purpose of our preference for high growth rates is to refine the microstructure and to reveal how growth rates affect the microstructure. Solidification at high growth rate during directional solidification results in grain refinement and microstructural evolution. It is known that the electrical, mechanical, and thermal properties of the alloy also change as a result of the change in the microstructure. From this point of view, it can be concluded whether it is an alloy (Al–Si–Ti) of which different properties (mechanical, electrical, *etc.*) can be improved. These results will contribute to control the directionally solidified alloys' microstructures which is in favor of the further application of Al–Si-based alloys.

II. EXPERIMENTAL PROCEDURE

In this work, the vast majority of the experimental part occurs in the sample preparation, performing directional solidification experiments, observing the microstructure, and measuring interflake eutectic spacings and solidification parameters for alloy. Another part is determining alloy thermophysical properties using differential scanning calorimetry (DSC). Details of these sections are given under headings.

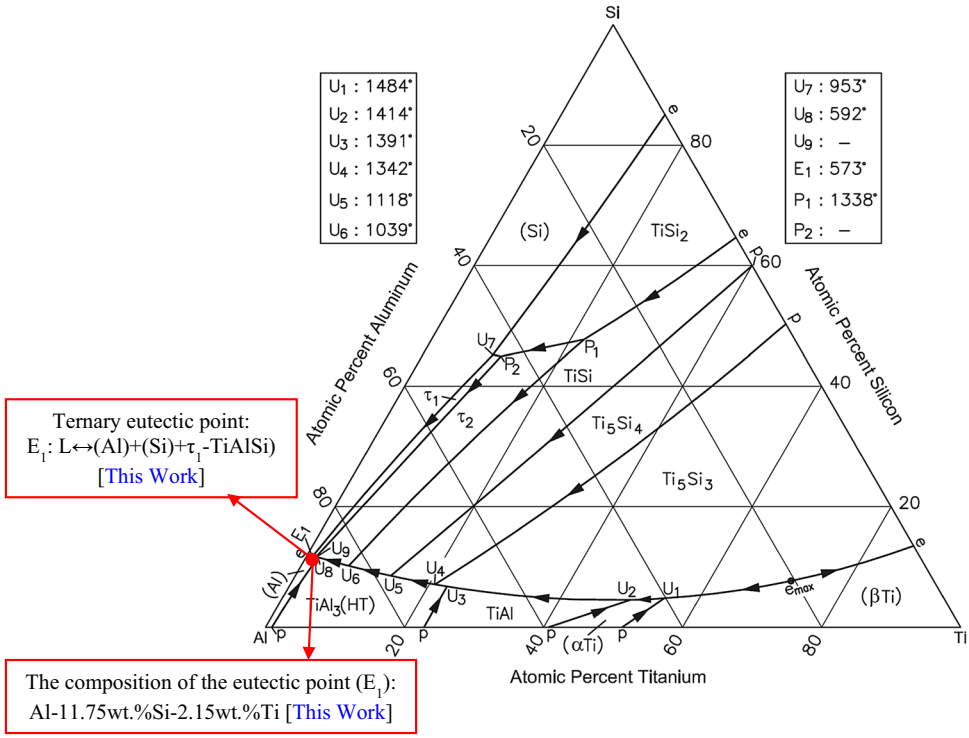

Fig. 1—Al-Si-Ti liquidus projection (reprinted from Ref. [54]—ASM International publication).

A. *Obtaining the Alloy, Directional Solidification Experiments, and Observation of the Microstructure*

At this stage of the study, the composition of the alloy, of which phase diagram is given in Figure 1, was chosen as Al–11.75wt pct Si–2.15 wt pct Ti. The eutectic alloy was prepared by melting 99.99 pct pure aluminum, 99.95 pct pure silicon, and 99.70 pct pure titanium in a vacuum melting furnace to grow other phases from the ternary liquid.

After making sure that the homogeneous alloy was formed, the molten alloy was poured into graphite crucibles (length: 200 mm, outer diameter: 6.35 mm, inner diameter: 4 mm) in another specially designed casting furnace with a temperature of approximately 100 °C above the melting temperature of the alloy. The molten alloy was directionally solidified to be completely filled into the crucible. Each obtained sample was then placed with a protective graphite cylinder (length: 300 mm, outer diameter: 40 mm, inner diameter: 10 mm) in the Bridgman-type directional solidification apparatus (BTDSA), the details, and block diagram which are given in the Figure 2. Directional solidification of the samples was conducted at a constant temperature gradient of 8.36 K mm^{-1} with eight different growth rates from 8.51 to 2065.18 $\mu m\ s^{-1}$ using synchronous motors with varying speeds of drawing.

Synchronous motors used in solidification experiments have pulling rates of 1, 2, 5, 10, 20, and 60 rps. The maximum achievable growth rate at a constant temperature gradient with a 60-rpm synchronous motor is 500.0 $\mu m\ s^{-1}$. To achieve the targeted growth rates (from ~ 212.45 to 2065.18 $\mu m\ s^{-1}$), a different driving system was designed by modifying a hand-drill motor. In Table I, pulling rates *vs* applied voltages or growth rates *vs* pulling rates are given using the designed drive system. Details of the experimental procedures and calculations and the Bridgman-type directional solidification apparatus (BTDSA) are given in Figure 2 and have been given in previous studies.[55–57]

To see the microstructures of the samples obtained with different growth rates, the following processes were applied briefly: After solidification, the quenched samples were removed from the graphite crucibles and cut into 15 mm lengths. Afterward, the parts of the transverse and longitudinal sections to be viewed were flattened with a few pieces of SiC paper, and cold mounting of the samples was made using epoxy resin. After polishing using different grits SiC papers and felts, it was finally etched with Keller's etchant (H_2O-95 mL, HNO_3-2.5 mL, HCl-1.5 mL, HF-1 mL) for 20–25 seconds. The microstructures of the samples were photographed with an Olympus BHX type light optical microscope (Integrated Olympus DP12 digital camera), and the alloy's phases are directly visible for all growth rates. Microstructure pictures of directional solidified samples of Al–Si–Ti alloy for both low and high growth rates are given in Figures 3 and 4, respectively.

In most cases, the results obtained by SEM–EDX analysis alone are sufficient to determine both phase identification and composition, but the true identities of the phases are all confirmed by analyzing the relevant X-ray diffraction patterns. In this study, after characterization of the alloy with SEM–EDX (Zeiss GeminiSEM 300) analysis, phases were verified with XRD (Bruker Discover 8) with CuKα1 (wavelength 1.5406 A) operating at 40 kV and 40 mA.

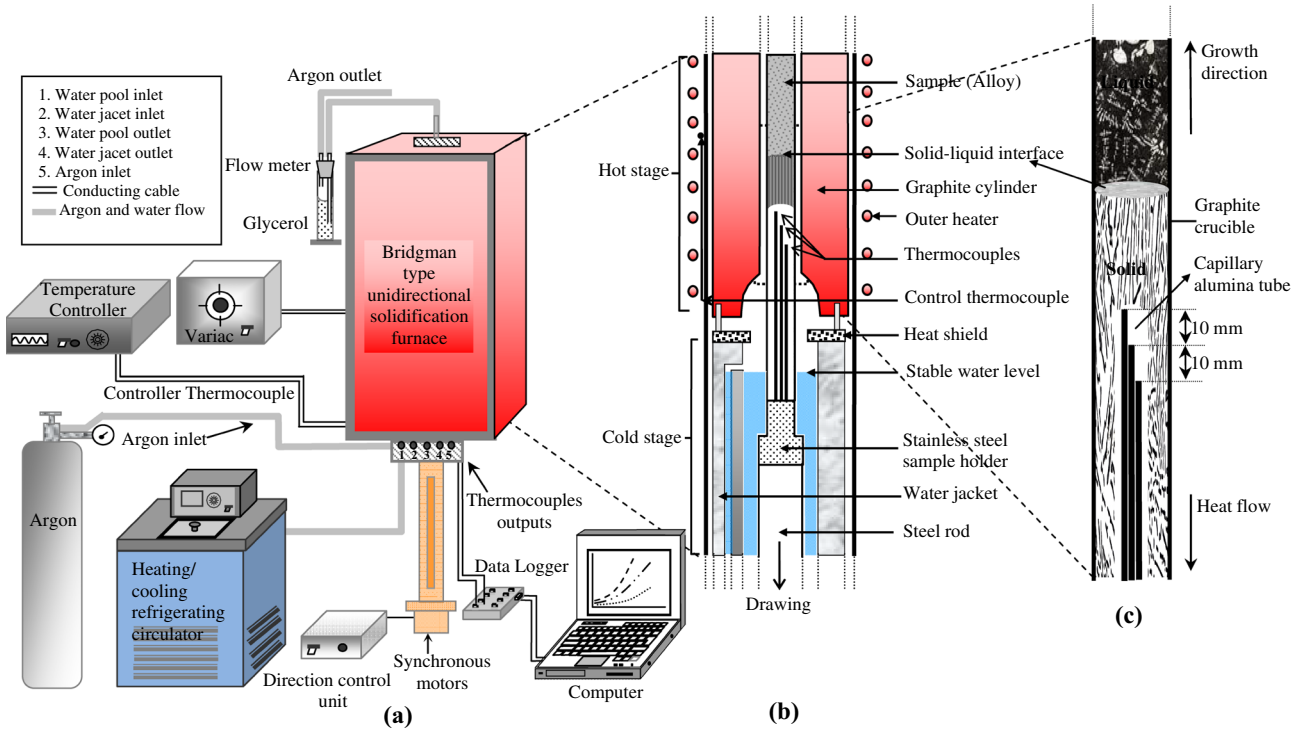

Fig. 2—(*a*) Block diagram of the experimental setup, (*b*) the details of the Bridgman-type directional solidification furnace, (*c*) the sample.

Table I. Applied Voltage *vs* Pulling Rates or Pulling Rates *vs* Growth Rates Obtained with Constructed Driving System for Al-11.75 Wt pct Si-2.15 Wt pct Ti Alloy

Applied Voltage (DC Volts)	Pulling Rate (μm/s)	Growth Rate (μm/s)
1.0	1073.45	504.53
2.1	2236.86	1042.14
2.9	3184.24	1552.38
3.8	4302.13	2065.18

B. *The Measurements of Interflake Eutectic Spacings and Solidification Parameters*

As shown in Figure 2(c), three K-type thermocouples (insulated with capillary ceramic alumina tube) of 0.25 mm diameter fixed to the samples at 10 mm distances were used to measure the temperatures inside the samples. Cooling rate values were recorded separately for each sample with a data logger connected to the computer. The growth rate values (V) were calculated by determining the time taken for the solid–liquid interface to pass through thermocouples fixed at 10 mm intervals ($V = \Delta X/\Delta t$).

The temperature gradient value (G) at the solid–liquid interface could be kept constant throughout the solidification experiments since the hotter region of the furnace and the cooler temperature and the distance between them were kept constant. The value of G was obtained by considering the temperature value of the third and second thermocouples ($G = \Delta T/\Delta X$). The details of getting the Δt, ΔX, and ΔT values used in the calculation of G and V are given in the studies in the relevant References 55 through 60.

The interflake eutectic spacings, λ_{Min} (the arithmetic average between minimum spacings), λ_{Max} (the arithmetic average between maximum spacings), and λ_T (the actual average spacings measured from the transverse section) values were obtained from optical microscope photographs of the longitudinal section (parallel to the pulling direction) and transverse section (perpendicular to the pulling direction) by making 50 measurements from at least five different regions for each sample. The schematic representation of the details of the measurements is shown in Figure 5. As seen in previous studies,[61,62] measurements taken from transverse sections were considered in this study since measurements made in transverse sections for λ values are more dependable than measurements made in longitudinal sections. Average data for λ_{Min}, λ_{Max}, and λ_T measurements, as well as other important results (such as solidification parameters, bulk growth rates, and equational relations) for Al–11.75 wt pct Si–2.15 wt pct Ti alloy are given in Table II.

C. *Determination of the Alloy Thermophysical Properties (ΔC_p and ΔH_f)*

DSC trace was used to obtain thermophysical properties such as ΔC_p (specific heat difference between solid and liquid) and ΔH_f, the fusion enthalpy or specific melting heat or the heat of fusion (the required energy for melting of the unit mass) of the eutectic alloy. Al–Si–Ti alloy was heated to approximately 1100 K

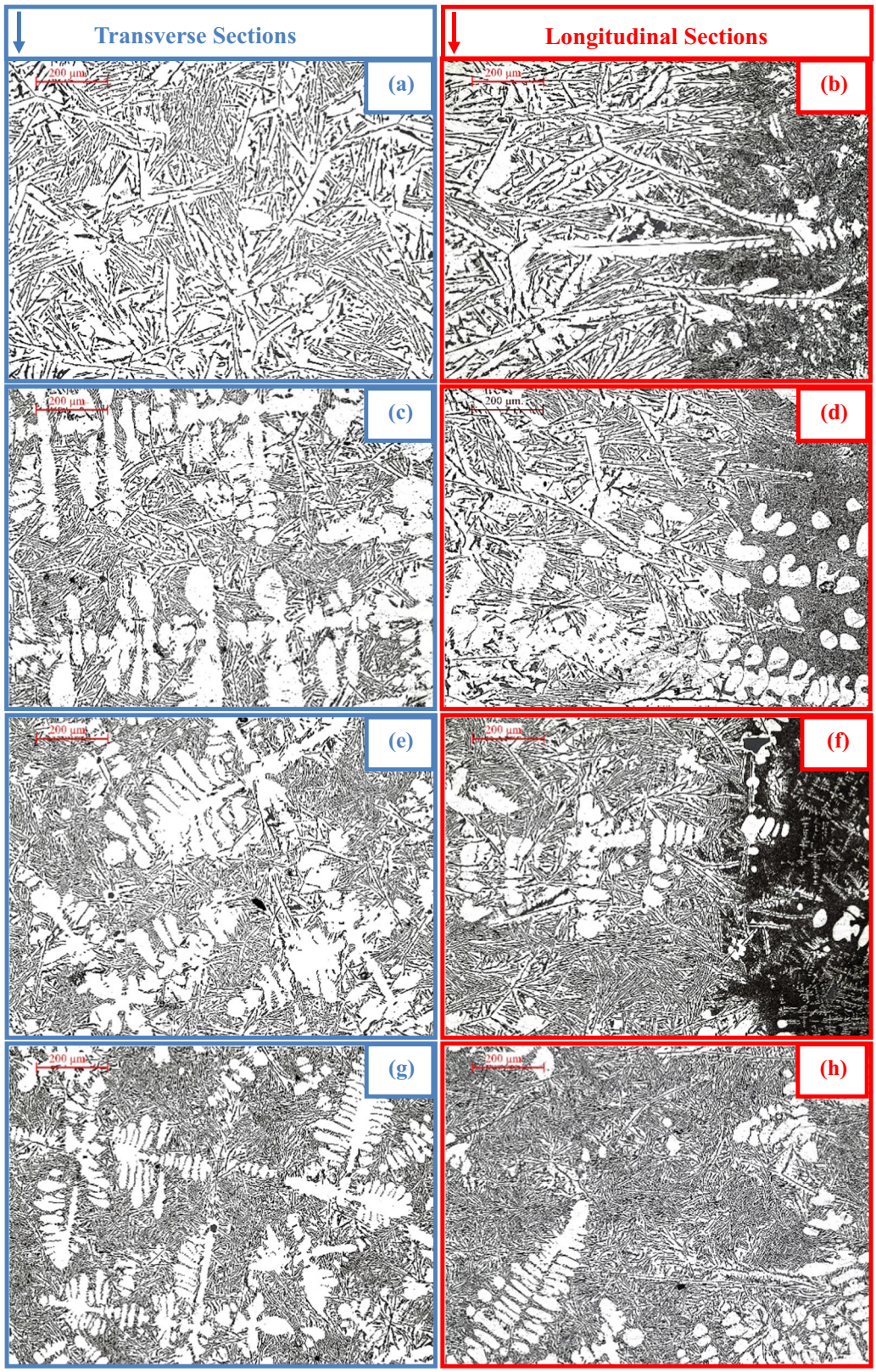

Fig. 3—The optical images of the growth morphologies of directionally solidified Al–11.75 wt pct Si–2.15 wt pct Ti eutectic alloy with low growth rates (V = 8.51—168.42 μm/s) at a constant temperature gradient (G = 8.36 K/mm). V = 8.51 μm/s (*a*) and (*b*), 43.15 μm/s (*c*) and (*d*), 85.58 μm/s (*e*) and (*f*), 168.42 μm/s (*g*) and (*h*), respectively.

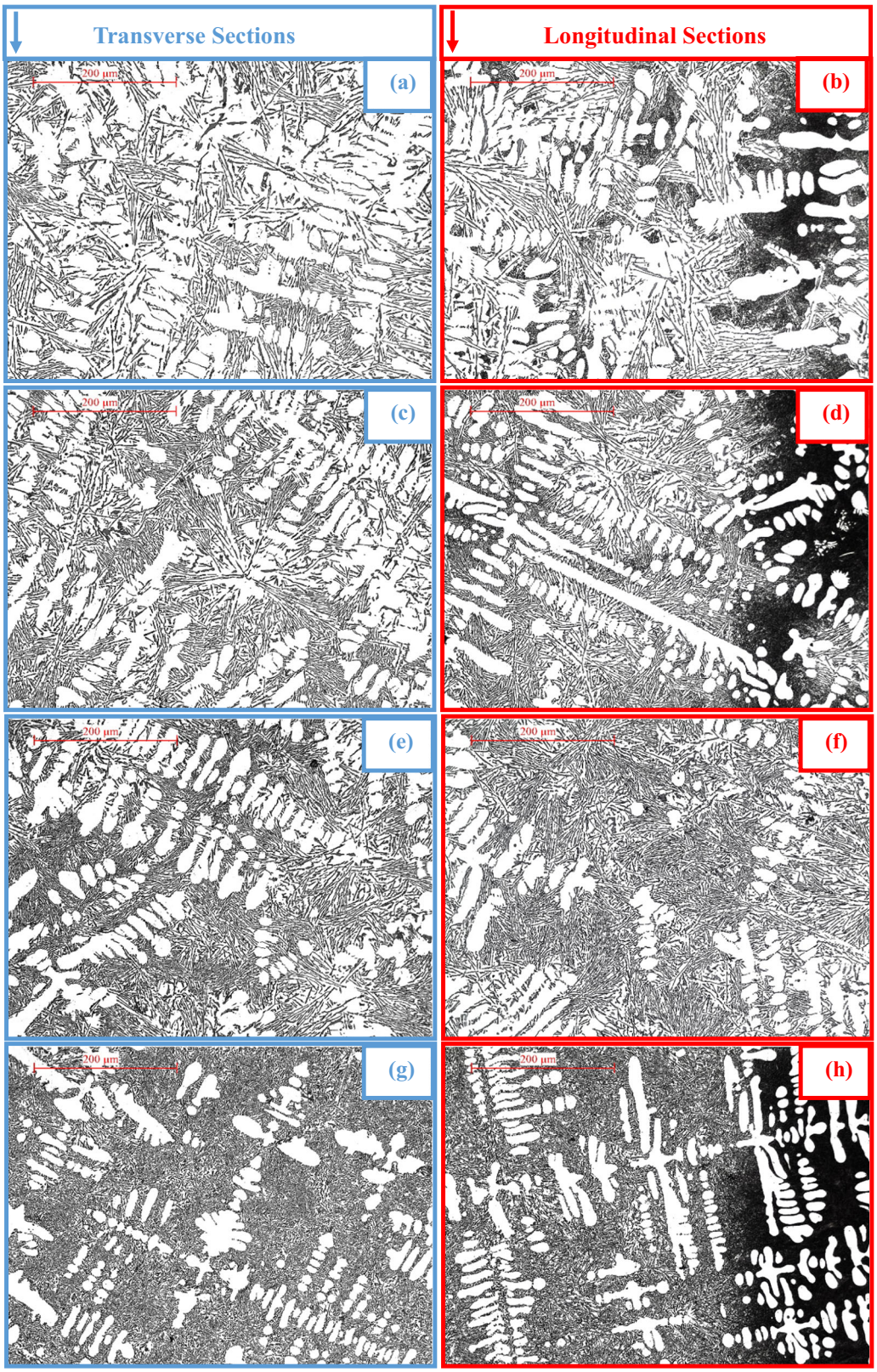

Fig. 4—The optical images of the growth morphologies of directionally solidified Al–11.75 wt pct Si–2.15 wt pct Ti eutectic alloy with high growth rates (V = 504.53—2065.18 μm/s) at a constant temperature gradient (G = 8.36 K/mm). V = 504.53 μm/s (*a*) and (*b*), 1042.14 μm/s (*c*) and (*d*), 1552.38 μm/s (*e*) and (*f*), 2065.18 μm/s (*g*) and (*h*), respectively.

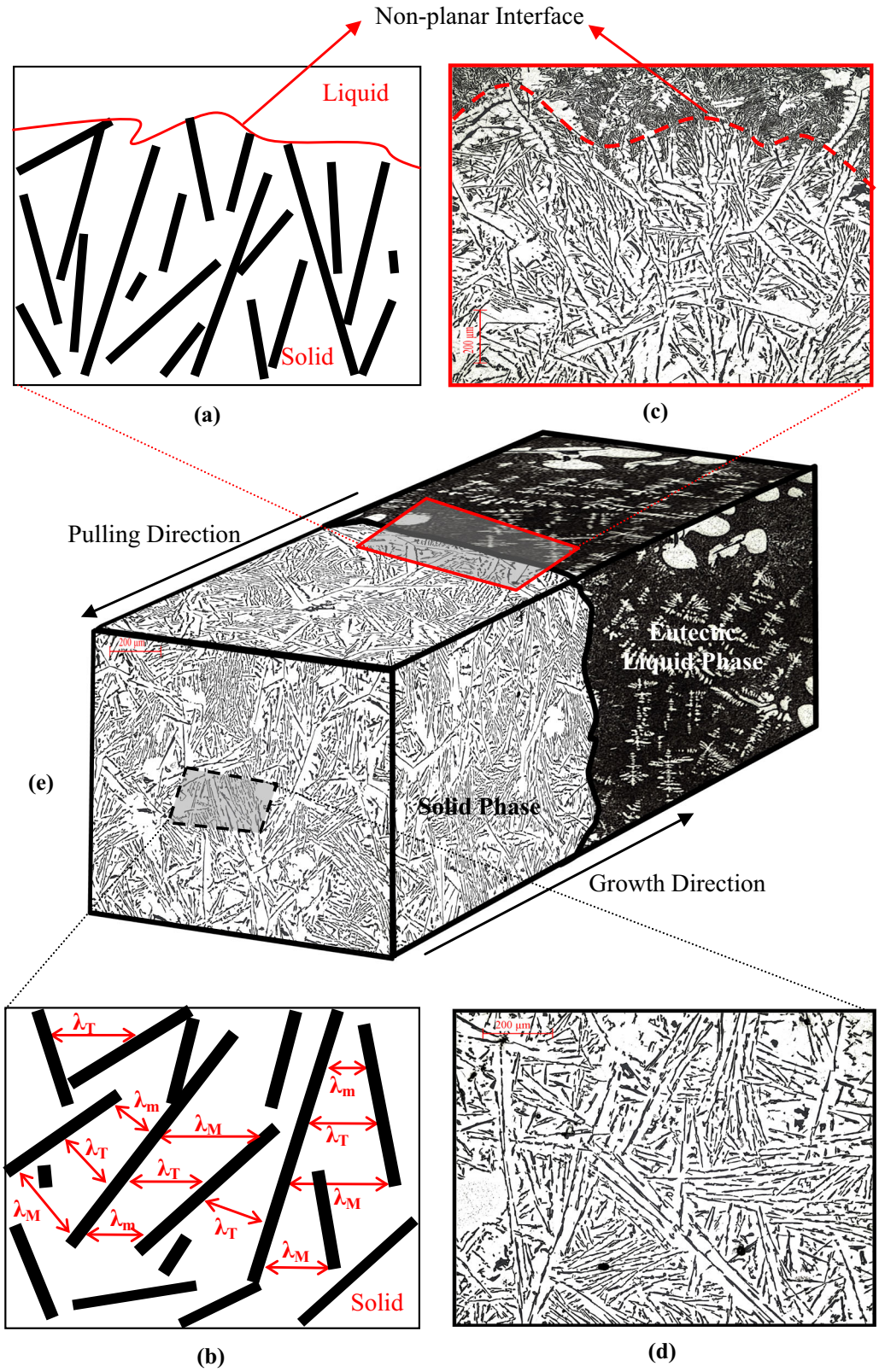

Fig. 5—(*a*) and (*b*) The schematic illustration and (*c*) and (*d*) a view of the longitudinal and transverse sections for the selected areas and also (*e*) the schematic illustration of the irregular growth on quenched sample (*e*). (Interflake eutectic spacing (λ_T) measurements from the transverse section for directionally solidified Al–Si–Ti eutectic alloy. (b)).

Table II. Solidification Processing Parameters (a), Interflake Spacings (a), Bulk Growth Rates (b), and Relationships (b) for Directional Solidified Al-Si-Ti Eutectic Alloy

(a)

Solidification Parameters		Interflake Spacings		
G (K/mm)	V (μm/s)	λ_{Min} (μm)	λ_{Max} (μm)	λ_T (μm)
8.36	8.51	5.81 ± 0.59	19.31 ± 1.25	12.56 ± 0.78
	43.15	2.20 ± 0.38	10.04 ± 0.96	6.12 ± 0.63
	85.58	1.75 ± 0.29	7.53 ± 0.82	4.64 ± 0.52
	168.42	1.22 ± 0.24	4.94 ± 0.63	3.08 ± 0.39
	504.53	0.98 ± 0.18	2.92 ± 0.51	1.95 ± 0.25
	1042.14	0.63 ± 0.14	2.59 ± 0.40	1.61 ± 0.23
	1552.38	0.47 ± 0.12	2.31 ± 0.32	1.39 ± 0.19
	2065.18	0.33 ± 0.10	2.23 ± 0.29	1.28 ± 0.16

(b)

	Low Growth Rates	High Growth Rates	All Growth Rates
Range of Growth Rates (μm s^{-1})	8.51–168.42	504.53–2065.18	8.51–2065.18
Average of Bulk Growth Rates $\lambda^2_T V$ (μm^3 s^{-1})	1599.71	2750.69	2175.20
Relationship [$\lambda = k\ V^{-n}$] (for a constant G)	$\lambda_{LGR} = k_1\ V^{-0.46}$	$\lambda_{HGR} = k_2\ V^{-0.30}$	$\lambda_{ALLGR} = k_3\ V^{-0.42}$
Constant (k)	$k_1 = 34.28\ \mu m^{1.46}\ s^{-1.46}$	$k_2 = 12.82\ \mu m^{1.30}\ s^{-1.30}$	$k_3 = 29.44\ \mu m^{1.42}\ s^{-1.42}$
Correlation Coefficient (r)	$r_1 = -0.997$	$r_2 = -0.995$	$r_3 = -0.996$

λ_{Min}: the arithmetic average between minimum spacings measured from the transverse section.
λ_{Max}: the arithmetic average between maximum spacings measured from the transverse section.
λ_T: the actual average spacings measured from the transverse section.

with a heating rate of 10 K/min. The ΔC_p value is referred to as ($\Delta C_p = \Delta H_f / T_M$) where T_M is the melting temperature of the alloy. As a result, using the DSC data of the alloy, firstly, ΔH_f value was obtained from the area under the peak. Afterwards, the ΔC_p value in the equation was calculated with the help of ΔH_f and T_M values.

III. RESULTS AND DISCUSSIONS

A. *Morphological Analysis and Evaluation of Microstructure*

The main purpose of this study is to reveal the relationship between low (LGRs), high (HGRs), and all growth rates (ALLGRs) and interflake eutectic spacings (λ_{Min}, λ_{Max}, and λ_T) in Al–Si–Ti eutectic alloy. In other words, it is to observe how the microstructure changes with unidirectionally solidified samples of Al–Si–Ti eutectic alloy in BTSDA at a wide range of growth rates (8.51 to 2065.18 μm s^{-1}) at a constant temperature gradient (8.36 K mm^{-1}) and to calculate the change mathematically.

Considering the phase diagram liquid projection of the Al–Si–Ti alloy (Fig. 1, reprinted from Ref.[54]), this system contains one eutectic point. Therefore, it was decided to choose the composition of the alloy as Al–11.75 wt pct Si–2.15 wt pct Ti (E_1). The eutectic reaction and phases at this point are as follows: Eutectic reaction; E_1: L $\leftrightarrow$ (Al) + (Si) + τ_1-TiAlSi, α-Al (matrix phase) solution, eutectic-Si phase, τ_1-TiAlSi (intermetallic phase). Microstructure photographs obtained from an optical microscope for different growth rates are given in Figures 3 and 4. The quantitative chemical composition analyses of all phases observed in the microstructure were performed using Energy Dispersive X-Ray Analysis (EDX), and the results are obtained as in Figure 6. The black phase is the eutectic-Si phase, the white phase is the matrix phase (α-Al), and the gray phase is the τ_1-TiAlSi ternary phase. Compositions of α-Al matrix phase and eutectic-Si phase in the microstructure confirm the previous literature studies.[9,11,15] As can be seen from Figure 6, the τ_1-TiAlSi intermetallic phase, which has a high melting point (953 °C < T < 1000 °C),[63] was also observed in some local areas from the longitudinal section of samples. Additionally, the Al–56.06 at. pct Si–33.38 at. pct Ti composition obtained for the τ_1 ternary phase was found to be consistent with the EDX results of both Liu *et al.*[63] and Li et al. (τ_1 phase; space group: $I4_1/amd$, structure type: $Zr_3Al_4Si_5$)[64] in the literature.

Figure 7 shows the X-ray diffraction pattern of the eutectic alloy. Diffrac Suite EVA software equipped with the current ICDD PDF-2 database was used for the determination of phases. The percentage quantities of elements were obtained from the XRD pattern of the alloy as follows: 85.0, 12.8, and 2.2 for Al, Si, and Ti, respectively. These values agree both the SEM–EDX results in this study and the composition given for the

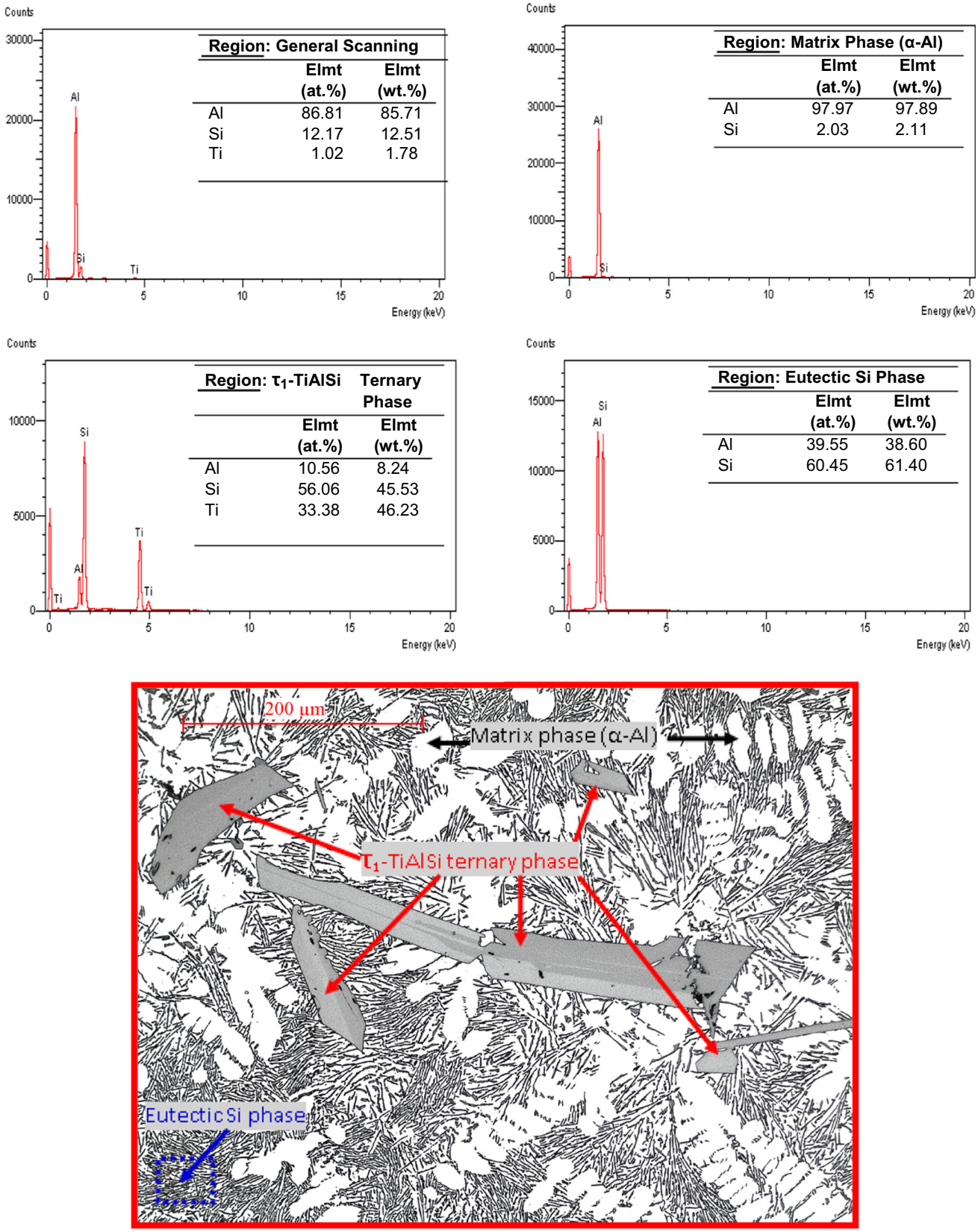

Fig. 6—The chemical composition analysis of Al–11.75 wt pct Si–2.15 wt pct Ti eutectic alloy by using SEM EDX. Black phase is eutectic-Si phase, white phase is matrix phase (α-Al) and gray phase is τ_1-TiAlSi ternary phase. (The value of growth rate for optic photograph is 1042.14 μm/s).

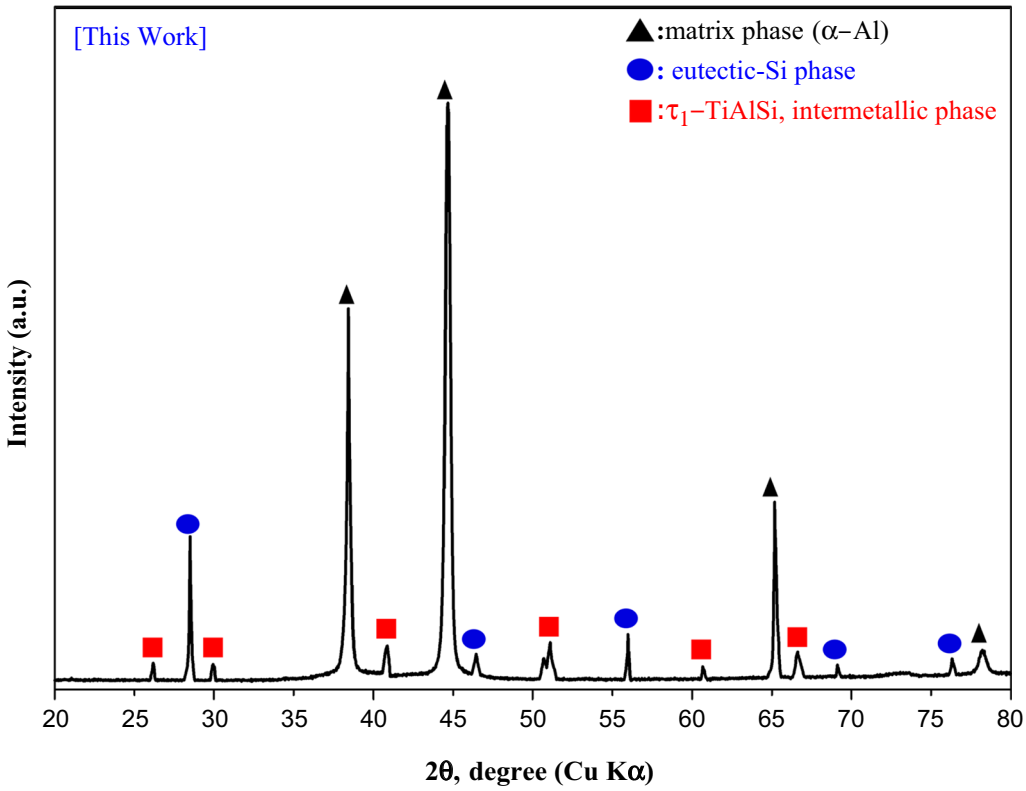

Fig. 7—X-ray diffraction pattern of Al–11.75 wt pct Si–2.15 wt pct Ti eutectic alloy (for 1042.14 μm/s).

eutectic point (E_1) in the literature.[63,64] The characteristic peaks of each phase: 38.48, 44.67, 65.17, 78.21 deg (for the α-Al matrix phase), 28.50, 46.44, 55.99, 69.12, 76.31 deg (for the eutectic-Si phase), 26.19, 29.95, 40.88, 51.09, 60.67, and 66.62 deg (for the τ_1-TiAlSi intermetallic phase). Li *et al.*[64] reported three strong peaks in the X-ray diffraction pattern for τ_1 phase: 2θ = 40.87, 51.01, and 66.64 deg, respectively. In addition, Gao *et al.*[65] investigated the τ_1 phase both theoretically and by heat treating Ti–Al–Si alloys at 595 °C for different times. In conclusion, the characteristic peaks obtained for the τ_1 phase in this study agree with little differences from the results reported by Li *et al.*[64] and Gao *et al.*[65]

B. *The Dependence of Interflake Eutectic Spacings on Low, High, and All Growth Rates*

The variations in growth rates affect the interflake spacing values. This work concluded that the interflake eutectic spacings decrease with the increase of the growth rates in a constant temperature gradient (G = 8.36 K mm^{-1}) and vice versa. As can be seen from Figures 3, 4 and Table II, the highest interflake spacing (12.56 μm) was obtained at the lowest growth rate (8.51 μm s^{-1}), and the lowest interflake spacing (1.28 μm) was measured at the highest growth rate (2065.18 μm s^{-1}).

The variation of eutectic interflake spacing with growth rate in logarithmic scale is linear up to a certain growth rate value (~ 400 μm s^{-1}), and the proportionality equation can be obtained by linear regression analysis as follows:

$$\lambda = K_1 \cdot V^{-n} \text{ (for constant } G\text{)}, \quad [1]$$

where K_1 is a constant and n is an exponent value of growth rate.

The relationships between growth rates and the interflake eutectic spacings (λ_{Min} and λ_{Max}) obtained from the transverse section were determined for directionally solidified Al–11.75 wt pct Si–2.15 wt pct Ti eutectic alloy, respectively (Figure 8);

$$\lambda_{Min} = 14.86\ V^{-0.47} \text{(for minimum interflake spacings)}, \quad [2a]$$

$$\lambda_{Max} = 44.69\ V^{-0.41} \text{(for maximum interflake spacings)}. \quad [2b]$$

In addition, the equations obtained depending on the low, high, and all growth rates (LGRs, HGRs, and ALLGRs) of the average interflake spacings (λ_T) are as follows: respectively (Figure 9):

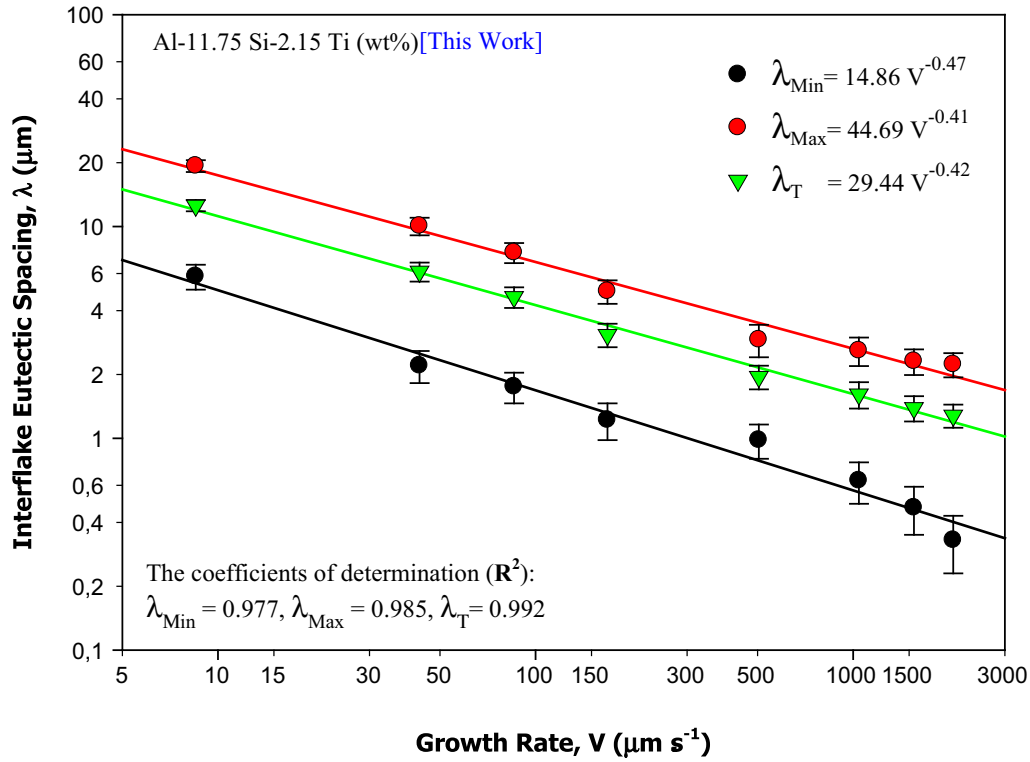

Fig. 8—Variation of minimum (λ_{Min}), maximum (λ_{Max}), and average (λ_T for all growth rates) interflake eutectic spacings as a function of growth rates for Al–Si–Ti eutectic alloy.

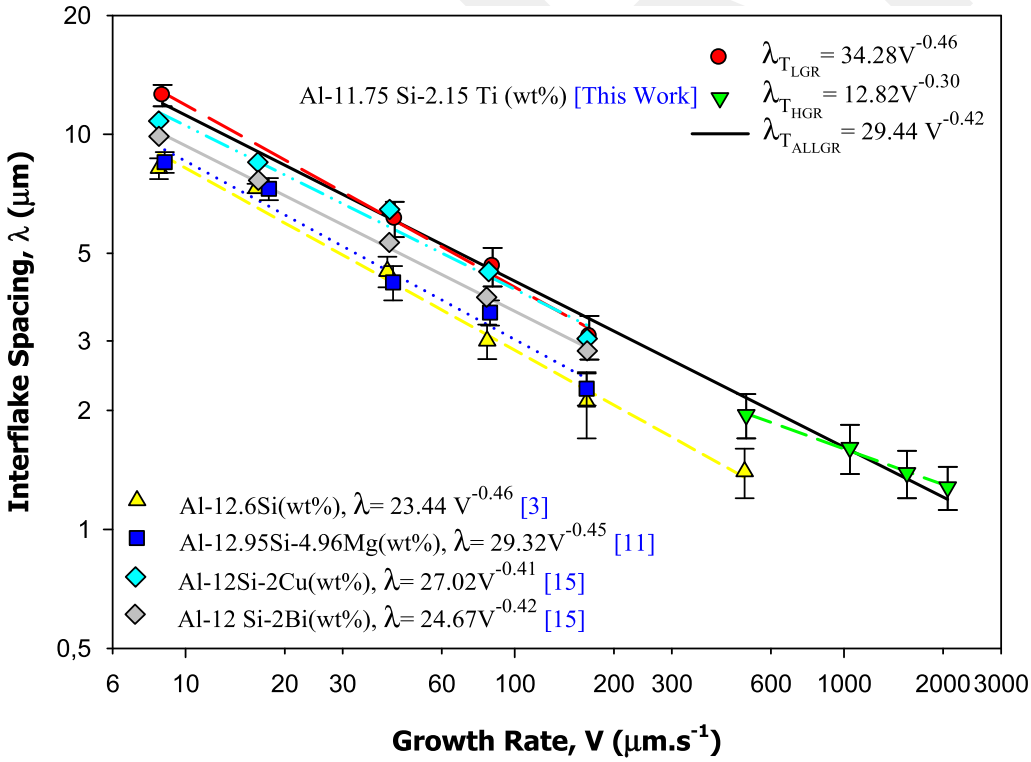

Fig. 9—Variation of the interflake spacings as a function of growth rates for directionally solidified Al–Si–Ti eutectic alloy at a constant temperature gradient and comparison of experimental present results with experimental results of previous Al–Si-based alloys.

$$\lambda_{T_{LGR}} = 34.28\ V^{-0.46} (\text{for low growth rates}), \quad [3a]$$

$$\lambda_{T_{HGR}} = 12.82\ V^{-0.30} (\text{for high growth rates}), \quad [3b]$$

$$\lambda_{T_{ALLGR}} = 29.44\ V^{-0.42} (\text{for all growth rates and average interflake spacings}). \quad [3c]$$

Many studies in the literature to classify the several types of microstructures produced by solidifying alloys with compositions close to the eutectic points. Jackson and Hunt ($\lambda^2 \cdot V =$ Constant or $\lambda = k \cdot V^{-0.50}$[66] put forward a helpful study that helps us to understand the structure of binary eutectic alloys and the growth kinetics of phases. This work[66] relates the eutectic structure in binary systems to the nature of the growth of their individual phases. Since there is no accepted theoretical model for the exponential value of ternary eutectic systems, binary and ternary alloys based on Al and Al-Si binary systems are taken and shown in Figure 9 and Table III to compare the experimental results obtained in this study.

As can be seen from Figure 8, the exponential value of 0.47 obtained for λ_{Min} values by Gündüz *et al.*[3] for Al–Si, Çadırlı *et al.*[10] for Al–Cu–Co, Kaygısız and Maraşlı.[11] for Al–Si–Mg, Aker *et al.*[67] for Al–Sb, and Fan *et al.*[68] for Al–Si–Ti was obtained in agreement with the exponential values 0.46, 0.45, 0.44, 0.45, and 0.44, respectively. At the same time, its closeness to the 0.50 value determined by the Jackson–Hunt model[66] shows that just like binary eutectic alloys, the eutectic-Si phases tend to get closer to each other proportionally with increasing growth rates (for λ_{Min}). The exponential value (0.41) obtained at the maximum interflake spacings (λ_{Max}) is close to the exponential values of some Al-Cu-based alloys[4,22] and different Al-Si-based alloys studied by Kaya and Aker[15] in the literature (0.39 for Al–Cu,[4] 0.41 for Al–Cu–Ti,[22] 0.41, 0.40, 0.43, 0.43, and 0.42 for Al–Si–Cu, Al–Si–Co, Al–Si–Ni, Al–Si–Sb, and Al–Si–Bi, respectively[15]). In addition, this exponential value (0.41) explains that as the distance between Si phases increases, the disorder will increase, and the alloy will move away from the eutectic structure form (See Figures 3 and 4).

The lines of λ_{LGR} *vs* V for low growth rates (0.46) determined in the present work are slightly below the lines of λ *vs* V determined by Kaya *et al.*[5] for Al–Ni (0.50), Böyük *et al.* for Al–Cu–Ag (0.49),[8] and for Al–Si–Ni (0.50)[9] and predicted from the Jackson–Hunt eutectic theory[66] (0.50). Considering that the growth rates are in a similar range, the difference here is due to the type, and amount of alloying elements added. This value is also in good agreement with the exponential values obtained by Gündüz *et al.*[3] for Al–Si (0.46), Bayram and Maraşlı[16] for Al–Cu–Ni (0.48), Fan *et al.*[68] for Al–Si–Ti (0.44), Wilde *et al.*[69] for Al–Cu–Ag (0.46), Kaygısız and Maraşlı[11] for Al–Si–Mg (0.45), and for Al–Cu–Si–Mg (0.46)[13] based on the spacings between eutectic phases. This agreement obtained for Si eutectic phases from the studies in the

Table III. A Comparison of the Values of Solidification Parameters and Microstructure for Directionally Solidified Al–Si–Ti Eutectic Alloy Obtained in Present Work with the Similar Values for Al-Based Alloys Obtained in Previous Works

Alloy (wt pct)	G (K/mm)	Range of λ (μm)	Range of V (μm/s)	Relationship	References
Al–11.75Si–2.15Ti	8.36	12.56–3.08	8.51–168.42	$\lambda_{T_{LGR}} = 34.28\ V^{-0.46}$	[This Work]
		1.95–1.28	504.53–2065.18	$\lambda_{T_{HGR}} = 12.82\ V^{-0.30}$	
		12.56–1.28	8.51–2065.18	$\lambda_{T_{ALLGR}} = 29.44\ V^{-0.42}$	
Al–12.6Si	7.80	8.2–1.4	8.30–498.70	$\lambda_{Si} = 23.44\ V^{-0.46}$	3
Al–33Cu	5.84	3.36–0.78	9.52–483.20	$\lambda_T = 22.10\ V^{-0.39}$	4
Al–5.7Ni	4.02	3.49–0.45	8.32–483.25	$\lambda_T = 10.76\ V^{-0.50}$	5
Al–2Li	6.06	83.44–40.06	8.30–164.70	$\lambda_a = 125.60\ V^{-0.25}$	6
Al–4.5Cu	8.8	90–7.5	10–240	$\lambda_1 = k\ V^{-0.38}$	7
Al–0.53Zn		1141–957	10–200	$\lambda_{min} = 731.30\ V^{-0.38} \lambda_{max} = 8671.40\ V^{-0.53}$	
Al–0.26Mn					
Al–17.57Cu–42.16Ag	8.79	3.86–0.51	8.30–498.25	$\lambda_\alpha = 11.22\ V^{-0.49}$	8
Al–11.1Si–4.2Ni	5.82	~ 7.5–0.9	4.60–243.33	$\lambda_{Si} = 12.58\ V^{-0.50}$	9
Al–23.9Cu–1.2Co	5.66	~ 4.8–1.1	8.30–166.60	$\lambda_T = 12.02\ V^{-0.44}$	10
Al–12.95Si–4.96 Mg	9.39	8.50–2.27	8.64–165.20	$\lambda_{Si} = 29.32\ V^{-0.45}$	11
Al–6.5Ni–1.5Fe	4.48	3.55–0.73	8.25–164.80	$\lambda_T = 10.80\ V^{-0.53}$	12
Al–28Cu–6Si–2.2 Mg	6.88	3.07–0.79	9.63–173.50	$\lambda_{Si} = 8.74\ V^{-0.46}$	13
Al–12Si–2Cu	8.06	10.80–3.04	8.28–165.80	$\lambda_{Si} = 27.02\ V^{-0.41}$	15
Al–12Si–2Co	7.98	6.14–1.82	8.30–166.08	$\lambda_{Si} = 16.02\ V^{-0.40}$	
Al–12Si–2Ni	7.88	8.26–2.72	8.32–165.92	$\lambda_{Si} = 21.05\ V^{-0.43}$	
Al–12Si–2Sb	8.04	9.12–2.57	7.98–165.95	$\lambda_{Si} = 23.69\ V^{-0.43}$	
Al–12Si–2Bi	8.12	9.88–2.83	8.30–165.94	$\lambda_{Si} = 24.67\ V^{-0.42}$	
Al–32.5Cu–0.6Mn	8.10	1.28–0.44	8.40–166.20	$\lambda_T = 3.02\ V^{-0.36}$	17
Al–26Cu–6.5Si–0.5Fe	8.5	~ 9.5–2	8.25–164.80	$\lambda_{Si} = 25.13\ V^{-0.55}$	20

literature indicates that for low growth rates, Al–Si-based eutectic alloys will grow in a form suitable for the Jackson–Hunt eutectic theory model.[66]

As can be seen from the previous studies in Table III, the exponential value of 0.30 obtained for high growth rates is away from both the Al-based eutectic alloys in the literature and the Jackson–Hunt eutectic model.[66] Considering the current eutectic theory[66] and the Al-based eutectic alloys referenced in this study, it can be concluded that this important difference is due to the high growth rates rather than the Si and Ti elements that consist the alloy. However, the exponent value (0.30) of V for λ_{HGR} is close to with the values of 0.26, 0.28, 0.26, 0.28, 0.32, and 0.33 reported by the other researchers[70–75] for Al–7Ni, Al–1.9Mn–5Fe, Al–5Cu–3 Mg, Al–1Zn, Al–3Cu, and Al–0.15 Mg–0.33 Si (at. pct) alloys, respectively. As a result of this consistency obtained for Al-based alloys without eutectic composition, high growth rates cause the microstructure to change and move away from the eutectic structure form. It was found that the pulling rate was like the growth rates, which may be because the metal sample holder and the graphite crucible had good thermal conductivity. It can be seen from Table I that after 400 μm s^{-1} growth rates, the growth rate values are approximately half of the draw rate values. This situation, encountered when the standard growth rate values in the literature are exceeded, reveals that the irregularity in the microstructure also increases due to the inability to respond quickly enough to the increase in pulling rates. More research work is necessary for better understanding of the morphologies and mechanisms responsible for the microstructure change in Al–Si–Ti alloys for high growth rates.

Finally, the value of 0.42 obtained from the measurements of the interflake eutectic spacings obtained for all growth rates agrees with the exponential values (0.41–0.40–0.43–0.43–0.42,[15] 0.45,[11] 0.44,[68] 0.42[76]) of the Al–Si-based alloys studied by Kaygısız and Maraşlı[11] (Al–Si–Mg), Kaya and Aker[15] (Al–Si–Cu, Al–Si–Co, Al–Si–Ni, Al–Si–Sb, and Al–Si–Bi), Fan *et al.*[68] (Al–Si–Ti), and Steinbach and Ratke[76] (Al–Si–Mg). However the experiments were not performed at high growth rates. In the study by Kaya and Aker[15] conducted in the standard growth rate range, the different elements added to the Al–12 wt pct Si eutectic alloy change the microstructure and other properties. Considering this harmony, the following conclusion can be drawn: it turns out that the elements added to the Al–Si binary eutectic increase the disorder in the microstructure more than the growth rates.

Si phases emerge as irregular structures with the unidirectional solidification of the Al–Si–Ti ternary eutectic (Figures 3 and 4) and may form colony-shaped structures with an increase in growth rate. Thus, with a large kinetic undercooling, growth protrudes in front of the interface, preventing simultaneous growth and forming regularly aligned structures. As a result of these reasons, the exponential values obtained for Si eutectic phases may deviate from the 0.50 expected value in the Jackson–Hunt eutectic model.[66] Jackson and Hunt[66] attribute this to the high $\Delta S/R$ (R gas constant and ΔS fusion entropy) value for the Al–Si eutectic case (3.59).

The bulk growth rate average values ($\lambda^2 V =$ Constant) were obtained as 1599.71 μm^3 s^{-1}, 2750.69 μm^3 s^{-1}, and 2175.20 μm^3 s^{-1} for low, high, and all growth rates, respectively.

C. *Determination of the Specific Heat (ΔC_p) and the Enthalpy of Fusion (ΔH_f) for the Al–Si–Ti Eutectic Alloy*

6,764 mg of Al–Si–Ti alloy obtained from castings was placed in the Perkin Elmer Diamond model *DSC* device and then heated from 400 to 1100 K with a heating rate of 10 K min^{-1} and a heat flow trace *vs* the temperature of the eutectic alloy was obtained. (Figure 10).

The melting temperature of the Al–Si–Ti ternary eutectic alloy was measured as 843.83 K in Figure 10, and this value is very close to the 846 ± 2 K value determined by Liu *et al.*[63] for the eutectic melting point. ΔC_P and ΔH_f for the Al–Si–Ti were determined to be 0.659 J g^{-1} K^{-1} and 376.12 J g^{-1}. As shown in Figure 10 and Table IV, the ΔC_P value is slightly smaller than only the 0.716 value obtained by Böyük *et al.*[77] for Al–Si–Ni but approximately two or three times greater than for other alloys. For example, ΔC_P values given for the Al–Cu–Co,[10] Al–Cu–Ni,[19] Al–Cu–Ti,[24] Al–Cu–Ag,[81] Al–Si–Cu,[82] and Al–Cu–Mn[83] in Figure 10 are 0.374, 0.422, 0.266, 0.433, 0.304, and 0.272 J g^{-1} K^{-1}, respectively. Likewise, it is seen in Table IV that the enthalpy of fusion (ΔH_f) value measured in this study is higher than both Al–Cu [10,19,24,78,81,83] and Al–Si [82]-based alloys.

IV. CONCLUSIONS

Al–Si-based Al–11.75 wt pct Si–2.15 wt pct Ti irregular eutectic alloy, primarily preferred in casting alloys and industry, was directionally solidified with a wide range of growth rates (V = 8.51 to 2065.18 μm s^{-1}) at a constant temperature gradient using BTDSA. Then, the microstructure images were taken, and the equations between the low, high, and all growth rates and the measured interflake eutectic spacings were obtained with the help of linear regression analysis. The results obtained here can be briefly summarized as follows:

I. The exponential value of 0.46 obtained for the directionally solidified Al–11.75 wt pct Si–2.15 wt pct Ti alloy at low growth rates (V = 8.51 to 168.42 μm s^{-1}) is quite close to the exponential values similar alloys in the literature and predicted by the Jackson and Hunt[66] eutectic theory model. However, looking at the exponential value (0.30) at high growth rates (V = 504.53 to 2065.18 μm s^{-1}), it is almost half the value of 0.50 in both the literature and the eutectic theory model.[66] After this comparison, it is seen that the Jackson and Hunt[66] eutectic

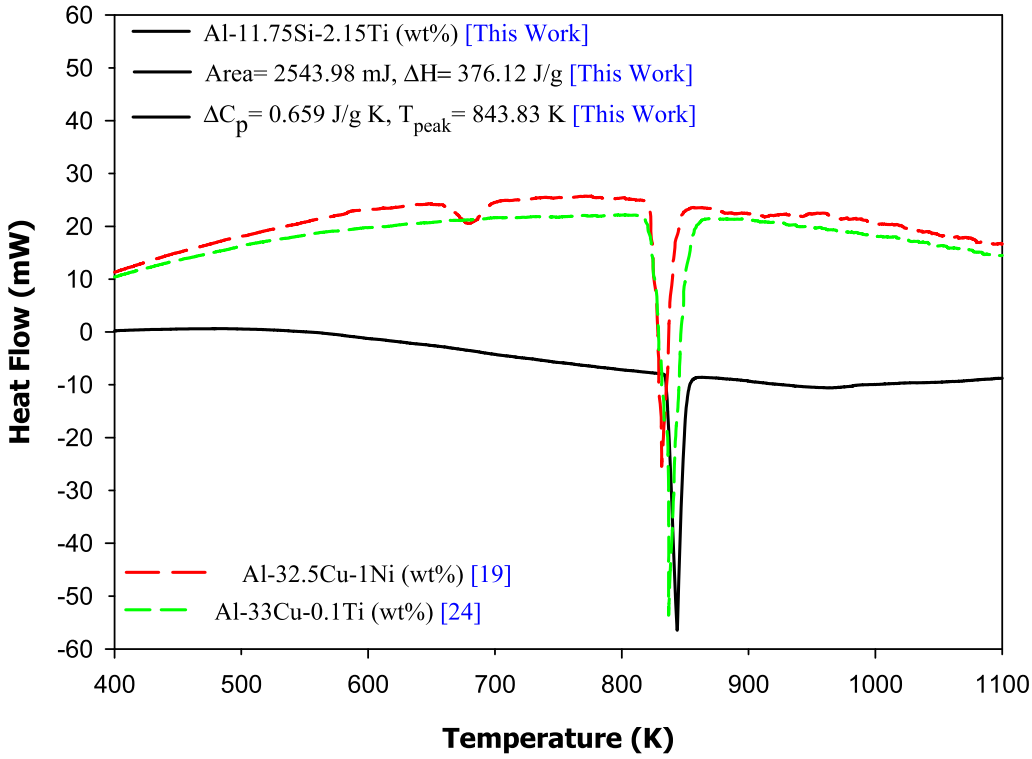

Fig. 10—Heat flow curve *vs* the temperature for the Al–Si–Ti eutectic alloy at a heating rate of 10 K/min.

Table IV. A Comparison of the Thermal Properties for Directionally Solidified Al-Si-Ti Eutectic Alloy Obtained in Present Work with Thermal Properties for Al-Based Alloys Obtained in Previous Works

Alloy (wt pct)	The enthalpy of fusion (ΔH) (J/g)	The specific heat (ΔC_p) (J/gK)	The melting temperature (K)	References
Al–11.75Si–2.15Ti	376.12	0.659	843.83	[This Work]
Al–23.9Cu–1.2Co	204.80	0.374	820.50	10
Al–32.5Cu–1Ni	235.63	0.422	831.53	19
Al–33Cu–0.1Ti	222.69	0.266	837.13	24
Al–11.1Si–4.2Ni	411.03	0.716	837.73	77
Al–3Cu	390.10	0.422	924.30	78
Al–6Cu	312.50	0.379	823.50	
Al–15Cu	287.40	0.349	823.90	
Al–24Cu	264.30	0.321	822.80	
Al–33Cu	252.20	0.307	821.30	
Al–5.7Ni	53.43	0.236	917.90	79
Al–7.5Ni	83.28	0.283	941.45	80
Al–17.6Cu–42.2Ag	223.80	0.433	789.70	81
Al–12.6Si–2Cu	260.84	0.304	857.53	82
Al–12.6Si–2Co	235.61	0.271	867.25	
Al–12.6Si–2Ni	209.31	0.244	856.68	
Al–12.6Si–2Sb	282.60	0.326	866.37	
Al-12.6Si–2Bi	248.05	0.285	870.11	
Al–1.9Mn–0.5Cu	182.60	0.272	944.20	83
Al–1.9Mn–1.5Cu	154.70	0.232	937.10	
Al–1.9Mn–5.0Cu	166.70	0.254	928.60	

theory differs for ternary alloys in the high growth rate range and increases in irregularity due to the inability of the interface to respond fast enough to the pulling rate.

II. The value of 0.42, which includes all growth rates (V = 8.51 to 2065.18 μm s^{-1}), agrees with the exponential values of some Al–Si-based alloys[11,15,68,76] in the literature, although they are solidified at standard growth rates (~ V = 7.98 to

166.08 μm s^{-1}). This comparison gives us the following result: the additional elements made to the Al–Si binary eutectic alloy affect the irregular growth (deviation from the eutectic structure) in the microstructure more than the growth rates.

III. Finally, the thermophysical properties of the Al–11.75 wt pct Si–2.15 wt pct Ti irregular eutectic alloy were determined using the DSC device; 843.83 K (melting temperature of alloy), 0.659 J g^{-1} K^{-1} (specific heat ΔCp), and 376.12 J g^{-1} (enthalpy of fusion ΔH_f).

ACKNOWLEDGMENTS

Since the experimental processes of this study were carried out in Erciyes University Science Faculty Solid State Physics-I laboratory, the researchers are thankful to the laboratory supervisor Professor Necmettin Maraşlı and his team for their support.

CONFLICT OF INTEREST

On behalf of all authors, the corresponding author states that there is no conflict of interest.

REFERENCES

1. D.A. Porter and K.E. Easterlirng: *Phase Transformations in Metals and Alloys*, 2nd ed. CRC Press, Boca Raton, 1992.
2. F.L. VerSnyder and R.W. Guard: *Tans. ASM*, 1960, vol. 52, pp. 485–92.
3. M. Gündüz, H. Kaya, E. Çadırlı, and A. Özmen: *Mater. Sci Eng. A*, 2004, vol. 369, pp. 215–29.
4. E. Çadırlı, A. Ülgen, and M. Gündüz: *Mater. Trans.*, 1999, vol. 40, pp. 989–96.
5. H. Kaya, U. Böyük, E. Çadırlı, and N. Maraşlı: *Kovove Mater.*, 2010, vol. 48, pp. 291–300.
6. H. Kaya, E. Çadırlı, and M. Gündüz: *Appl. Phys. A*, 2009, vol. 94, pp. 155–65.
7. X. Lin, W.D. Huang, J. Feng, T. Li, and Y. Zhou: *Acta Mater.*, 1999, vol. 47, pp. 3271–80.
8. U. Böyük, N. Maraşlı, H. Kaya, E. Çadırlı, and K. Keşlioğlu: *Appl. Phys. A*, 2009, vol. 95, pp. 923–32.
9. U. Böyük, S. Engin, and N. Maraşlı: *Mater. Charact.*, 2011, vol. 62, pp. 844–51.
10. E. Çadırlı, İ Yılmazer, M. Sahin, and H. Kaya: *Trans. Indian Ins. Met.*, 2015, vol. 68, pp. 817–27.
11. Y. Kaygısız and N. Maraşlı: *J. Alloys Compd.*, 2015, vol. 618, pp. 197–203.
12. S. Engin, U. Böyük, and N. Maraşlı: *J. Alloys Compd.*, 2016, vol. 660, pp. 23–31.
13. Y. Kaygısız and N. Maraşlı: *J. Alloys Compd.*, 2017, vol. 721, pp. 764–71.
14. F. Bertelli, E.S. Freitas, N. Cheung, M.A. Arenas, A. Conde, J. de Damborenea, and A. Garcia: *J. Alloys Compd.*, 2017, vol. 695, pp. 3621–31.
15. H. Kaya and A. Aker: *J. Alloys Compd.*, 2017, vol. 694, pp. 145–54.
16. Ü. Bayram and N. Maraşlı: *Metall. Mater. Trans. B*, 2018, vol. 49B, pp. 3293–3305.
17. Y. Kaygısız: *China Foundry*, 2018, vol. 15, pp. 390–96.
18. R. Kakitani, R.V. Reyes, A. Garcia, J.E. Spinelli, and N. Cheung: *J. Alloys Compd.*, 2018, vol. 733, pp. 59–68.
19. N. Maraşlı and Ü. Bayram: *J. Alloys Compd.*, 2018, vol. 753, pp. 695–702.
20. U. Böyük, S. Engin, H. Kaya, E. Çadırlı, and N. Maraşlı: *Phys. Met. Metall.*, 2020, vol. 121, pp. 78–83.
21. E. Çadırlı, E. Nergiz, H. Kaya, U. Büyük, M. Sahin, and M. Gündüz: *Int. J Cast Met. Res.*, 2020, vol. 33(1), pp. 11–23.
22. Ü. Bayram and N. Maraşlı: *Phys. Metals Metallogr.*, 2020, vol. 21, pp. 382–90.
23. E. Üstün and E. Çadırlı: *J. Alloys Compd.*, 2021, vol. 855(1), p. 157331.
24. N. Maraşlı and Ü. Bayram: *Int. J. Thermophys.*, 2021, vol. 42, p. 94.
25. H. Kaya, U. Büyük, E. Çadırlı, M. Sahin, and M. Gündüz: *J. Mater. Eng. Perform.*, 2022, vol. 31, pp. 1622–30.
26. W. Kurz and D.J. Fisher: *Fundamentals of Solidification, Chapter 5*, 4th revised Trans Tech Publications Ltd., Bäch, 1998.
27. Y.S. Sun, G.W. Lorimer, and N. Ridley: *Metall. Trans. A*, 1990, vol. 21A, pp. 575–88.
28. Y. Zhang, C. Song, L. Zhu, H. Zheng, H. Zhong, Q. Han, and Q. Zhai: *Metall. Mater. Trans. B*, 2011, vol. 42, pp. 604–11.
29. R. Kakitani, G.L. de Gouveia, A. Garcia, N. Cheung, and J.E. Spinelli: *J. Therm. Anal. Calorim.*, 2019, vol. 137, pp. 983–96.
30. T. Duffar and L. Sylla: *Crystal Growth Processes Based on Capillarity. Chapter 6—Vertical Bridgman Technique and Dewetting*, Wiley, New York, 2010, pp. 355–411.
31. R. Venkataraman: *Handbook of Radioactivity Analysis. Chapter 4—Semiconductor detectors*, Elsevier Inc., Amsterdam, 2020, pp. 458–59.
32. C. Baron, H. Springer, and D. Raabe: *Mater. Des.*, 2016, vol. 112, pp. 131–39.
33. S.Q. Ma, J.D. Xing, H.G. Fu, Y.M. Gao, and J.J. Zhang: *Acta Mater.*, 2012, vol. 60, pp. 831–43.
34. C. Baron, H. Springer, and D. Raabe: *Mater. Sci. Eng. A*, 2018, vol. 724, pp. 142–47.
35. G. Xu, K. Wang, X. Dong, L. Yang, H. Jiang, Q. Wang, and W. Ding: *Metall. Mater. Trans. A*, 2020, vol. 51A, pp. 4610–22.
36. V.Y. Bazhin, V.M. Sizyakov, A.A. Vlasov, and R. Yu Feshchenko: *Metallurgist*, 2013, vol. 56, pp. 863–66.
37. I.V. Uskov, S.V. Belyaev, I.D. Uskov, T.R. Gilmanshina, I.V. Kirko, and N.P. Koptseva: *ARPN J. Eng. Appl. Sci.*, 2016, vol. 11, pp. 12367–70.
38. N.A. Belov, N.O. Korotkova, T.K. Akopyan, and A.M. Pesin: *J. Alloys Compd.*, 2019, vol. 782, pp. 735–46.
39. S. Birinci, S. Basit, and N. Maraşlı: *J. Mater. Eng. Perform.*, 2022, vol. 31, pp. 5070–79.
40. S. Hegde and K.N. Prabhu: *J Mater Sci.*, 2008, vol. 43, pp. 3009–27.
41. A. Pacz, 1921, U.S. Patent No: 1387900.
42. K. Nogita and A.K. Dahle: *Mater. Trans. (JIM)*, 2001, vol. 42, pp. 207–14.
43. Y. Zhang, F. Yan, Y. Zhao, C. Song, and H. Hou: *Mater. Res. Express*, 2020, vol. 7, p. 036526.
44. G.S. Vinod Kumar, B.S. Murty, and M. Chakraborty: *J. Alloys Compd.*, 2005, vol. 396, pp. 143–50.
45. K.P. Rao and Y.J. Du: *Mater. Sci. Eng. A*, 2000, vol. 277, pp. 46–56.
46. T. Gao, P. Li, Y. Li, and X. Liu: *J. Alloys Compd.*, 2011, vol. 509, pp. 8013–17.
47. N. Saheb, T. Laoui, A.R. Daud, M. Harun, S. Radiman, and R. Yahaya: *Wear*, 2001, vol. 249, pp. 656–62.
48. G. Zhang, W. Su, and A. Suzumura: *Metall. Mater. Trans. B*, 2016, vol. 47B, pp. 2026–39.
49. J.C. Pang, X.P. Cui, A.B. Li, G.H. Fan, L. Geng, Z.Z. Zheng, and Q.W. Wang: *Mater. Sci. Eng. A*, 2013, vol. 579, pp. 57–63.
50. I.A. Alkadir: *DJES*, 2016, vol. 9(4), pp. 48–61.
51. A.D. Subhi, A.A. Khleif, and Q.S. Abdul-Wahid: *Eng. Trans.*, 2020, vol. 68, pp. 385–95.
52. L. Chen, J. Xu, and X. Chun Li: *Mater. Res. Lett.*, 2015, vol. 3(1), pp. 43–49.
53. W. Kurz and R. Trivedi: *Metall. Trans. A-Phys. Metall. Mater. Sci.*, 1991, vol. 22(12), pp. 3051–57.
54. V. Raghavan: *J. Phase Equilib. Diffus. ASM Int.*, 2009, vol. 30, pp. 82–83.
55. E. Çadırlı and M. Gündüz: *J. Mater. Proc. Technol.*, 2000, vol. 97, pp. 74–81.

56. M. Asta, C. Beckermann, A. Karma, W. Kurz, R. Napolitano, M. Plapp, G. Purdy, M. Rappaz, and R. Trivedi: *Acta Mater*, 2009, vol. 57, pp. 941–71.
57. E. Acer, H. Erol, and M. Gündüz: *Light Met. Technol. Book Ser. Mater. Sci. Forum*, 2013, vol. 765, pp. 215–19.
58. E. Çadırlı, H. Kaya, and M. Gündüz: *Mater. Res. Bull.*, 2003, vol. 38, pp. 1457–76.
59. Ü. Bayram, Y. Karamazı, P. Ata, S. Aksöz, K. Keşlioglu, and N. Maraşlı: *Int. J. Mater. Res.*, 2016, vol. 107, pp. 1005–15.
60. E. Çadırlı, H. Kaya, and N. Maraşlı: *Met. Mater. Int.*, 2009, vol. 15, pp. 741–51.
61. H. Kaya, E. Çadırlı, and M. Gündüz: *J. Mater. Process Technol.*, 2007, vol. 183, pp. 310–20.
62. H. Kaya, E. Çadırlı, and M. Gündüz: *J. Mater. Eng. Perform.*, 2003, vol. 12, pp. 456–69.
63. S. Liu, F. Weitzer, J.C. Schuster, N. Krendelsberger, and Y. Du: *Int. J. Mater. Res.*, 2008, vol. 99, pp. 705–11.
64. Z. Li, C. Liao, Y. Liu, X. Wang, Y. Wu, M. Zhao, Z. Long, and F. Yin: *J. Phase Equ. Diffus.*, 2014, vol. 35, pp. 564–74.
65. M. Gao, T.J. Chen, and Z.X. Zhang: *J. Mater. Sci. Technol.*, 2021, vol. 94, pp. 247–63.
66. K.A. Jackson and J.D. Hunt: *Trans. TMS-AIME*, 1966, vol. 236, pp. 1129–42.
67. A. Aker, S. Engin, I. Yılmazer, and H. Kaya: *Int. J. Mater. Eng. Technol.*, 2013, vol. 9, pp. 59–79.
68. J. Fan, X. Li, Y. Su, J. Guo, and H. Fu: *J. Alloys Compd.*, 2010, vol. 506(2), pp. 593–99.
69. J. De Wilde, L. Froyen, and S. Rex: *Scr. Mater.*, 2004, vol. 51, pp. 533–38.
70. D.G. McCartney and J.D. Hunt: *Acta Metall.*, 1981, vol. 29, pp. 1851–63.
71. Berkdemir and M. Gündüz: *Mater. Sci. Forum*, 2010, vol. 649, pp. 425–30.
72. E. Çadırlı: *Met. Mater. Int.*, 2013, vol. 19, pp. 411–22.
73. H. Kaya, U. Böyük, E. Çadırlı, and N. Maraşlı: *Met. Mater. Int.*, 2013, vol. 19, pp. 39–44.
74. E. Acer, E. Cadirli, H. Erol, H. Kaya, and M. Gündüz: *Met. Mater. Trans. A*, 2017, vol. 48, pp. 5911–23.
75. E. Çadırlı, A. Aker, Y. Kaygısız, and M. Sahin: *Mater. Res.*, 2017, vol. 20, pp. 801–13.
76. S. Steinbach and L. Ratke: *Metall. Mater. Trans. A*, 2007, vol. 38A, pp. 1388–94.
77. U. Böyük: *Met. Mater. Int.*, 2012, vol. 18, pp. 933–38.
78. S. Aksöz, Y. Ocak, N. Maraşlı, E. Çadirli, H. Kaya, and U. Böyük: *Ex. Ther. Flu. Sci.*, 2010, vol. 34, pp. 1507–16.
79. H. Kaya, U. Böyük, E. Çadırlı, and N. Maraşlı: *Mater. Des.*, 2012, vol. 34, pp. 707–12.
80. A. Aker and H. Kaya: *Int J Ther.*, 2013, vol. 34, pp. 267–83.
81. U. Böyük, N. Maraşlı, E. Çadırlı, H. Kaya, and K. Keşlioğlu: *Curr. Appl. Phys.*, 2012, vol. 12, pp. 7–10.
82. A. Aker and H. Kaya: *Int. J. Cast Met. Res.*, 2017, vol. 30(5), pp. 293–300.
83. U. Büyük, E. Çadırlı, and H. Kaya: *EJONS Int. J. Math. Eng. Nat. Sci.*, 2022, vol. 6, pp. 18–27.